ELSEVIER

Applied Catalysis A: General 191 (2000) 205–220

APPLIED CATALYSIS A: GENERAL

www.elsevier.com/locate/apcata

The metal–support interaction in Pt/Y zeolite: evidence for a shift in energy of metal d-valence orbitals by Pt–H shape resonance and atomic XAFS spectroscopy

D.C. Koningsberger [a,*], J. de Graaf [a], B.L. Mojet [a,1], D.E. Ramaker [b], J.T. Miller [c]

[a] *Department of Inorganic Chemistry and Catalysis, Debye Institute, Utrecht University, P.O. Box 80083, 3508 TB Utrecht, The Netherlands*

[b] *Chemistry Department, George Washington University, Washington, DC 20052, USA*

[c] *BP Amoco Research Center, E-1F, 150 W. Warrenville Rd., Naperville, IL 60563, USA*

Received 29 June 1999; received in revised form 5 July 1999; accepted 6 July 1999

Abstract

The turnover frequency (TOF) for conversion of neo-pentane was determined for Pt in Y zeolite with different numbers of protons and La^{+3} ions, different Si/Al ratios and with non-framework Al being present. Comparing Pt/NaY to Pt/H-NaY and Pt/K-USY with Pt/H-USY, respectively, shows an increase in the ln (TOF) which is proportional to the number of protons. Compared to NaY, the TOF of Pt in non-acidic NaLaY zeolite is about 25 times higher, which indicates also a strong influence on the charge of the cations on the TOF of Pt. The 20 times increase in the Pt TOF for K-USY compared to NaY is attributed to the effect of a higher Si/Al ratio and non-framework Al in the K-USY.

EXAFS data collected on Pt/NaY and Pt/H-USY showed platinum particles consisting of 14–20 atoms on an average. These results were confirmed by HRTEM, which also showed that the Pt particles were dispersed inside the zeolite. The EXAFS data indicate that the metal particles are in contact with the oxygen ions of the support. The peak in the Fourier transform of the atomic XAFS (AXAFS) spectrum of the Pt/H-USY is larger in intensity than the corresponding peak of the Pt/Na-Y data. A detailed analysis of the L_2 and the L_3 X-ray absorption near edge structure revealed a shape resonance due to the Pt–H anti-bonding state (AS) induced by chemisorption of hydrogen on the surface of the platinum metal particles. The difference in energy (E_{res}) between the AS and the Fermi-level (E_F) is 4.7 eV larger for Pt/H-USY than for Pt/NaY. Both the AXAFS spectra and the shape resonances of the Pt-NaY and the Pt/H-USY catalysts provide direct experimental evidence of how the support properties determine the electronic structure of the platinum metal particles.

Previous AXAFS and shape resonance work lead to a model in which the position in energy of the Pt valence orbitals is directly influenced by changes in the potential (i.e. electron charge) of the oxygen ions of the support and how the proton density affects this oxygen charge. This work shows that the potential of the oxygen ions is also a function of the Si/Al ratio of the support and the polarisation power of the charge compensating cations (H^+, Na^+, La^{3+} and extra-framework Al); the metal particles experience an interaction which is determined by several properties of the support. The data further reveal how the change in the Pt electronic structure directly influences the catalytic properties of the catalyst.

While the TOF is dependent on the metal–support interaction, the hydrogenolysis selectivity is determined by the Pt particle size, and increases linearly with increasing dispersion, or decreasing particle size.

*Corresponding author.

[1] Present address: Schuit Institute of Catalysis, Eindhoven University of Technology, P.O. Box 513, 5600 MB Eindhoven, The Netherlands.

0926-860X/00/$ – see front matter
PII: S0926-860X(99)00320-8

Keywords: Metal–support interaction; Pt/Y; Pt/LaY zeolite; Pt/USY zeolite; Pt turnover frequency of neo-pentane; Atomic XAFS; Pt L_2 and L_3 near edge analysis; Pt–H anti-bonding state shape resonance; Oxygen charge

1. Introduction

Supported noble metal catalysts are used in a large number of commercially important applications, including hydrogenation, dehydrogenation, naphtha reforming, isomerisation, hydrocracking, oxidation, automotive exhaust catalysts and fuel cells [1]. While platinum is by far the most common catalytic metal, palladium, rhodium, iridium, and ruthenium are used in certain applications. A general review on supported metal clusters has recently been published [2].

Since the early work of Dalla Betta and Boudart [3], numerous studies have reported enhancements in the specific reaction rates for benzene hydrogenation [4,5], propane hydrogenolysis [6,7] and neo-pentane hydrogenolysis and isomerisation [3,7–9] on acidic supports compared to neutral supports. These differences were believed to be due to an interaction between the metal particles and the support. The metal–support interaction has been shown as not only altering the catalytic behaviour. There are indications that the metal–support interaction also changes the electronic properties of the supported metal cluster. Considering the catalytic results for competitive hydrogenation of benzene/toluene, Larsen and Haller suggested a decreased electron density on the platinum as the LTL zeolite acidity increased by cation exchange [10]. de Mallman and Barthomeuf proposed that the shift to lower frequency in the infrared spectra of adsorbed CO was due to a higher electron density of Pt on alkaline Y zeolite [11,12]. Finally, XPS data suggest that zeolite supported Pt and Pd clusters are electron deficient [13,14] on acidic supports and electron rich on alkaline supports [13,15].

Several explanations for the metal–support interaction have been proposed in the literature. The experimental basis of most explanations contains a lot of deficiencies and some explanations are more feasible than others:

1. *Formation of a metal–proton adduct* [8,16]. The formation of positively charged Pd–H^+ adducts for Pd in Y zeolite was proposed to account for the electron deficient particles observed in acidic zeolites. However, such adducts cannot account for an increase in electron density on the metal clusters in alkaline zeolites.
2. *Charge transfer between the metal atoms and the nearest neighbour zeolite oxygen atoms* [10–12,15]. It has been suggested that the Sanderson electronegativity of the nearby support oxygen atoms increases with increasing zeolite alkalinity [10,11]. The change in electronegativity of these support oxygen atoms would result in a charge transfer from or to the metal particles. However, Ponec et al. [17] argued that charge transfer is very unlikely.
3. *Polarisation of the metal particles by nearby cations* [18,19]. Calculations indicate that metal atoms near cations attract electrons, thus resulting in electron deficient metal atoms on the opposite side of the cluster. However, experiments underlying the theoretical calculations are lacking.

Systematic studies of Mojet et al. [13,20] have shown that the catalytic activity and spectroscopic properties of supported noble metal catalysts are greatly affected by the charge compensating cations (H^+, K^+) in LTL zeolite. As the K^+ content of the support increases, the turnover frequency (TOF) of the metal particles for neo-pentane hydrogenolysis decreases. At the same time, there is a decrease in the (Pd) XPS binding energy and a shift from linear to bridge bonded CO in the FTIR spectra of Pd and Pt. The XPS and the FTIR results are a strong indication of a direct influence of the support on the electronic properties of the metal particles. These effects were found to be independent of the metal (Pd or Pt). Although the influence of the support properties on the catalytic properties of the metal particles has been established, the nature of this interaction is still uncertain.

Recently, we have developed new analysis methods for the interpretation of two phenomena, which have been found to be present in X-ray absorption fine structure data of small platinum clusters dispersed in LTL zeolite: atomic XAFS (AXAFS) [21] and a shape resonance [22] due to the anti-bonding state (AS) of

the Pt–H interaction. The AXAFS spectra and shape resonances are found to be sensitive to changes in the binding energy of the Pt electrons. The AXAFS spectra reflect the average of all atoms present in the metal particles. However, the AS shape resonance reflects only on the platinum atoms present on the surface of the metal particles and is, therefore, directly related to the electronic properties of the catalytic active sites. Mojet et al. applied these Pt–H shape resonance [23] and the AXAFS techniques [24] to study the metal–support interaction in the Pt/LTL zeolites as described above. The AXAFS and shape resonance data were strongly dependent on the H^+ and K^+ contents of the LTL support. The results were explained by a Coulomb interaction between the metal particles and interfacial support oxygen ions, which affects the metal electron binding energies. This interaction causes a shift in the energy of the metal valence orbitals: the ionisation potential of the metal particles increases with increasing charge on the support oxygen atoms. This model for the metal–support interaction explicitly excludes the need for electron transfer. The model can account for all observed changes in the catalytic, electronic and structural properties of the supported metal particles that are induced by changes in the charge of the support oxygen brought about by different charge compensating cations (H^+, K^+).

In this paper, the validity of this model is explored further for platinum particles dispersed in Y zeolite. Expanding on the earlier work that examined the influence of H^+ versus K^+, we also study the influence of multivalent cations (La^{3+}), the Si/Al ratio and extra framework aluminum on both catalytic and electronic properties of the platinum particles. The results of the catalytic and XAFS studies (including EXAFS, AXAFS and Pt–H shape resonances) strongly support the model for the metal–support interaction as put forward by Mojet et al. [24]. The electron charge of the oxygen atoms is not only determined by the presence of H^+ versus K^+ on the support but also by the Si/Al ratio and the polarisation by multivalent cations and extra-framework aluminum.

Table 1
Elemental analysis of Pt/Y catalysts

Catalyst	wt.% Al	wt.% Na	wt.% La	wt.% Pt
Pt/NaY	11.1	10.1	–	2.0
Pt/H-NaY	11.5	5.2	–	2.0
Pt/K-USY	12.1	0.1 (6.2% K)	–	1.9
Pt/H-USY[a]	11.9	0.1	–	2.0
Pt/NaLaY (2%)	10.4	6.2	2.2	1.8
EXAFS samples				
Pt/NaY	11.1	10.1	–	0.9
Pt/H-USY[b]	11.9	0.1	–	0.6

[a] Prepared by Pt exchange from H-USY.
[b] Prepared by Pt exchange from NH_4-USY.

2. Experimental

2.1. Catalyst preparation

All supports were prepared from commercially available zeolites. NaY (LZY-54, UOP) was ion-exchanged with $La(NO_3)_3$ or NH_4NO_3. At low levels of exchangeable ions, nearly all $NH_4{}^+$ and La^{3+} ions were incorporated into the zeolite. Thus, for partial exchange, limited quantities of reagents were added. Commercial H-USY (LZY-84, UOP) was ion-exchanged with excess KNO_3 to obtain K-USY. Each support was washed and dried two times, and subsequently, calcined at 300°C for 3 h.

Platinum was added to each support by ion-exchange with $[Pt(NH_3)_4](NO_3)_2$ at 80°C. Exchange of NH_4USY was performed in the presence of NH_4NO_3 with ammonium as a competitive ion. After thorough washing, the catalysts were dried at 150°C and calcined at 250°C and reduced in flowing hydrogen at 250°C. The elemental analysis is given in Table 1. Pt dispersion was determined by hydrogen chemisorption and is given in Table 2.

2.2. Temperature programmed desorption (TPD) of NH_3

The number of acid sites was determined by TPD (heating rate 10° min^{-1} to 600°C for 1 h) for catalysts containing only chemisorbed NH_3. Approximately 1 g of catalyst was saturated in a flow of 5% NH_3/N_2 at room temperature. In order to remove physisorbed NH_3, the catalyst was washed three times in 50 ml H_2O at 80°C, filtered and dried at 100°C overnight. The quantity of desorbed NH_3 was determined by titration with a standard solution (0.1 M) of HCl. The number of protons was calculated based on the assumption that

Table 2
Number of acid sites, Pt dispersion, TOF and hydrogenolysis selectivity for the conversion of neo-pentane by Pt/Y catalysts

Catalyst	Acid sites (mmol g^{-1})	Pt dispersion	TOF[a]	Hydrogenolysis selectivity[b]
Pt/NaY	0.15	0.56	5.9×10^{-5}	0.56
Pt/H-NaY	1.96	0.36	5.0×10^{-4}	0.46
Pt/K-USY	0.16	0.40	1.2×10^{-3}	0.62
Pt/H-USY	1.61	0.23	7.7×10^{-3}	0.20
Pt/NaLaY (2%)	0.22	0.66	1.5×10^{-3}	0.93

[a] TOF = molecules per second surface Pt atom determined at 250°C, 1 atm and with 1% neo-pentane in H_2.
[b] Selectivity extrapolated to zero conversion and deactivation.

one NH_3 chemisorbed per acid site and the results are given in Table 2.

2.3. Neo-pentane hydrogenolysis

Neo-pentane hydrogenolysis was conducted in a fixed bed reactor at 250°C, using 0.99 vol.% neo-pentane in H_2. The catalysts were pre-reduced at 500°C for 1 h, and conversion was adjusted to values between 0.5 and 2.0% by varying space velocity. The initial conversion and selectivity were determined by extrapolation to time zero. The TOF (at time zero) was calculated based on H_2 chemisorption. Selectivities were calculated on a molar basis as the percent of neo-pentane converted to iso-pentane (isomerisation) and iso-butane plus methane (hydrogenolysis) extrapolated to zero conversion and deactivation. The analysis of the reaction products was carried out using the Delplot method [25], which gives, by extrapolation to zero conversion, the primary product distribution.

2.4. XAFS spectroscopy

2.4.1. Analysis of the platinum L_3 and L_2 X-ray absorption edges

The analysis method of the L_2 and L_3 white line areas is based upon several theoretical concepts, which are schematically viewed in Fig. 1 [22]. The spin–orbit interaction in both core and valence levels introduces differences between the L_3 ($2p_{3/2} \rightarrow 5d_{5/2}, 5d_{3/2}$) and L_2 ($2p_{1/2} \rightarrow 5d_{3/2}$) edges, both in shape and intensity (the $2p_{3/2}$–$2p_{1/2}$ splitting is around 1709 eV, and the $5d_{5/2}$–$5d_{3/2}$ splitting around is 1.5–2.5 eV [26]). The L_3 edge reflects the empty valence levels (ΔVB) of both $d_{5/2}$ and $d_{3/2}$ bands, weighted as $d_{5/2}/d_{3/2} = 6$ [26]; however, the L_2 edge reflects only the $d_{3/2}$ level. For small platinum clusters, $5d_{3/2}$ is believed to be completely filled due to band narrowing relative to platinum bulk; therefore, there is no Pt d valence band (ΔVB) contribution to the L_2 edge [22].

Hydrogen chemisorption induces a bonding and an anti-bonding orbital as reported by Hammer et al. [27] (see Fig. 2). The partially occupied 'dangling' platinum surface orbitals form a bond with the hydrogen 1s orbital producing the bonding and anti-bonding Pt–H orbitals. Since the Pt–H bonding orbital is primarily localised on the H atom, and the AS is localised more on the surface Pt atoms, the $5d_{3/2}$ component of the AS state is also assumed to shift below the Fermi level. However, the transition of the outgoing electron to the empty anti-bonding orbital should be evident in the near edge spectrum of the L_3 X-ray absorption edge (see Fig. 1). The AS can be viewed as a localised state degenerate with a continuum state, here, described by the Pt–H EXAFS final state wave function. The outgoing electron will reside temporarily in the potential well determined by the AS state and can escape undergoing a resonance with the Pt–H EXAFS final state wave function. This one electron process causes a shape resonance with the well known Fano-like resonance line shape. Its effect on the scattering cross section $\sigma(E)$ can be related to an EXAFS function $\chi(E)$ via the normal expression $\sigma(E) = \mu(E)(1 + \chi(E))$. It can be shown [22] that

$$\chi(E) = \frac{1}{k} A \sin\Phi \left[\frac{1 - q\varepsilon}{1 + \varepsilon^2} \right] \quad (1)$$

with A being an amplitude factor, $q = \cot\Phi$ and $\varepsilon = (E - E_{res})/\Gamma$. Φ can be related to the usual total phase found in EXAFS containing the $2kr$ term and the phase from the absorber and back-scatterer. ε is the normalised energy scale relative to the resonance

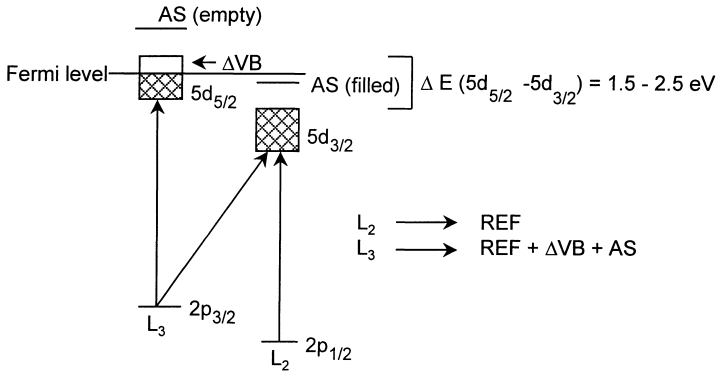

Fig. 1. Illustration of spin–orbital coupling effects in the X-ray absorption $L_{2/3}$ edge spectra and 5d valence band. REF: L_2 edge used as reference, AS: Pt–H AS, ΔVB: empty valence d-orbitals. The energy levels (2p and 5d) do not have the same scale.

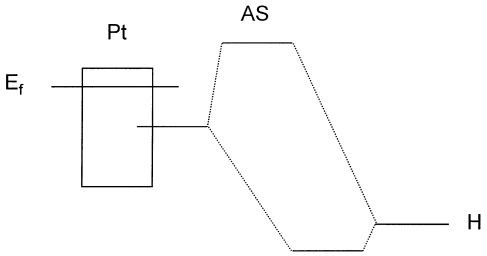

Fig. 2. Molecular orbital (MO) picture showing the formation of bonding and anti-bonding orbitals derived form a surface Pt orbital and the H 1s orbital.

Table 3
Main information present in the Pt L_3 and L_2 near edge spectra

Sample	L_3 edge	L_2 edge
H–Pt	REF + ΔXAFS + ΔVB + AS	REF + ΔXAFS
Pt	REF + ΔVB	REF

energy (E_{res}), whereby Γ represents the resonance width. A fit to the experimentally observed AS lineshape gives values for E_{res}, Γ, A and Φ.

Table 3 summarises the important contributions that will be visible in the four X-ray absorption edges of platinum in Pt/LTL catalysts, based on the assumptions and theory described above. The L_2 edge spectrum for 'clean' Pt clusters can be used as the reference (REF), since this spectrum arises from the 'free' atom absorption and the EXAFS contributions. The L_3 spectrum of the clean Pt cluster contains, in addition, the electronic (empty valence band: ΔVB) contribution. The L_2 spectrum for the H–Pt sample is different from the REF spectrum because of changes in geometry of the cluster induced by chemisorption of hydrogen (changes in XAFS scattering: ΔXAFS). Finally, the L_3 spectrum for the H–Pt sample contains both the geometric (ΔXAFS) and electronic (ΔVB + AS) changes from the reference [22].

Before the different contributions (ΔVB, ΔXAFS, AS) can be separated from the X-ray absorption spectra, the edges have to be aligned in order to account for initial and final state effects. All spectra are aligned relative to the reference, the L_2 edge spectrum being for clean Pt clusters. A detailed description of the physical principles that form the basis of the alignment procedure and a further discussion of the assumptions used in the analysis method described here are given in [22]. In short, both L_2 edges were aligned at 0.6 step height, whereas both L_3(H–Pt) and L_3(Pt) edges were aligned with the help of the EXAFS oscillations relative to the L_2 edges.

2.4.2. AXAFS

In the last few years, several research groups [28,29] have reported on the oscillatory structure detected in the atomic background μ_0 that is removed from the raw absorption data. It was first shown by Holland et al. [28] that $\mu_0(k) = \mu_{free}(k)(1 + \chi_{AX}(k))$, with μ_{free} being the free atomic background and $\chi_{AX}(k)$ being a fine structure attributed to AXAFS. As was pointed out by Rehr et al. [29], the AXAFS contribution will be visible as a peak in the Fourier transform at an unphysically short distance, often less than 1.5 Å.

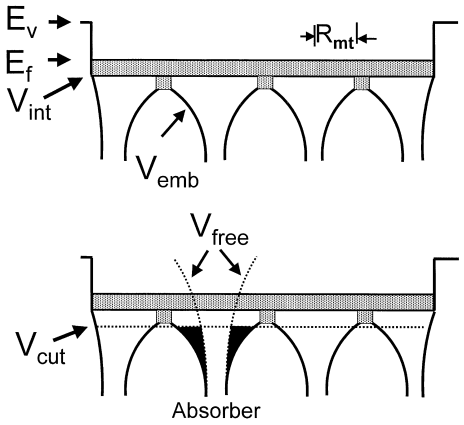

Fig. 3. (a) Illustration of the muffin-tin approximation to the interatomic potentials showing locations of V_{int} and E_F. (b) Schematic illustration of the shape and intensity of the Fourier transform of the AXAFS (black shaded area between V_{emb} and the free atom potential, V_{free}) and below V_{cut} as defined in the text.

Ramaker et al. [21] have recently discussed the origin and the parameters determining the AXAFS. The AXAFS is caused by the scattering of the photoelectron off the deep valence electrons in the periphery of the absorbing atom. From a more physical point of view, the photoelectron scatters against the embedded atom potential barrier. The well known muffin-tin approximation can be used to approximate the embedded atom potential. As illustrated in Fig. 3a, the muffin-tin approximation 'clips' the exact potential at the muffin-tin radius R_{mt} and sets it equal to the interstitial potential V_{int} [21]. Inside R_{mt}, the potential is assumed to be spherical, and outside R_{mt}, it is assumed to be flat and zero (i.e. no forces are exerted on the particle in the interstitial region). V_{int} is determined by averaging the potential at R_{mt} of all the atoms in the cluster, and this determines the zero of energy or the effective bottom of the conduction band.

A phase corrected and k weighted Fourier transform of $\chi_{AX}(k)$ leads to [21]

$$\left|\mathrm{FT}(k\mathrm{e}^{-2i\delta}\chi_{AX})\right| \approx \Delta V \times \Gamma \qquad (2)$$

where $\Delta V = V_{emb} - V_{TFA}$ with V_{emb} being the embedded atom potential, V_{TFA} the truncated free atom potential, and Γ a broadening function due to the limited Fourier transform range. The free atom potential reflects the electron distribution in the free atom, whereas the embedded potential reflects the electron distribution after embedding the free atom into its chemical environment and allowing interaction with its neighbors. Eq. (2) then reveals that the FT directly reflects this change in the chemical environment. More specifically, the shape and intensity of the |FT| can be represented by the black area between V_{TFA} and V_{emb} and below V_{cut} ($V_{cut} = 2 \times V_{int} + |E_F|$) as illustrated in Fig. 3b.

The scattering of the photoelectron by an electron in an orbital is primarily resonant, which implies that scattering occurs if the kinetic energy of the photoelectron is equal to the kinetic energy of the bound electron. On going upward above E_F in Fig. 3b, the linear kinetic energy of the photoelectron increases, while on going downward below V_{int}, the orbital kinetic energy of the valence electrons localised on a single atom increases. The photoelectron at the absorption edge already has a kinetic energy equal to E_F minus V_{int}. The electrons in the conduction band are not effective for scattering because they have a kinetic energy well below that of this photoelectron even at the threshold. Moreover, the electrons above V_{cut} have insufficient orbital kinetic energy. Thus, only electrons below V_{cut} (i.e. with higher binding energy) will be effective in scattering photoelectrons with kinetic energy well above the threshold. Only the *deeper localised* valence band electrons give rise to AXAFS scattering.

2.4.3. XAFS data collection

X-ray absorption spectra have been collected at station 9.2 of the Daresbury SRS. The station is equipped with a double crystal monochromator with Si (2 2 0) crystals. Higher harmonic radiation was removed from the incoming radiation by detuning the monochromator to 50% of the incoming intensity at a photon energy of 11564 eV (Pt L_3 edge). The spectra were collected in transmission mode, using two ion chambers filled with a gas mixture of Ar and He so that the total absorbance in the first chamber was 20% and that in the second chamber 80%. The samples were pressed into self-supporting wafers with a calculated thickness so that the total absorbance, μx, was 2.5 with an edge step of $\Delta\mu x \approx 0.2$. The samples were then mounted in an in-situ cell equipped with Be windows [30]. The EXAFS samples Pt/NaY and Pt/H-USY were reduced in flowing hydrogen at 400°C (heating rate 5°C min^{-1})

for 1 h. The samples were cooled under 1 atm. H_2. XAFS spectra were recorded at liquid nitrogen temperature. Subsequently, the samples were evacuated at 200°C for 1 h and XAFS spectra were recorded at liquid nitrogen temperature, maintaining a vacuum of better than 2×10^{-5} Pa.

2.4.4. XAFS data analysis methods

The absorption data was background subtracted using standard procedures. The pre-edge background was approximated by a modified Victoreen and removed from the raw data. The post-edge background was removed using a cubic-spline approximation [31] and the spectra were normalised on the absorption edge step height at 50 eV past the absorption edge. The isolation of the AXAFS and EXAFS signals from the smooth free atom background (the post-edge background removal) is important for a proper analysis of both AXAFS and EXAFS phenomena. We have previously defined new criteria [21,32] for background removal based on the procedure first outlined by Cook and Sayers [31]. Three criteria are defined for the Fourier transform spectra:

1. Diminish as much as possible the contribution at $R = 0.3$ Å.
2. Make sure that the EXAFS intensity at $R > 1.5$ Å is unchanged.
3. Check both k^1 and k^3 weighted spectra, for different k ranges, including low k values.

By using the above given criteria, the smooth atomic background and multi electron excitations are isolated from the AXAFS and EXAFS contributions to the spectrum.

Theoretical phase and backscattering amplitudes for the Pt–Pt and Pt–O scattering pairs were generated utilising the FEFF7 [33] code. The potential type, the real and imaginary contributions to the potential, S_0^2 and the Debye–Waller factor were varied until the generated references fitted optimally the first co-ordination shell of the experimental, background subtracted XAFS spectra for Pt foil [34] and $Na_2Pt(OH)_6$ [35] for the Pt–Pt and Pt–O references, respectively. More details on generating the theoretical references can be found in [32]. The theoretical references that we have generated can be used over a significantly lower k-range than the previously used experimental references. We were able to fit the χ_{EX} to a lower limit of about 2.5 $Å^{-1}$. The previously extracted and used experimental references were only usable for $k > 3.5$ $Å^{-1}$ due to Fourier filtering errors. The gain at low k is important for the analysis of the AXAFS phenomenon since the amplitude of the AXAFS oscillations decreases rapidly with increasing k. The result is a better isolation of the AXAFS peak at low R.

The XAFS data has been analysed using the program XDAP [36]. Fitting is done in R-space, without Fourier filtering of the data. This will result in more reliable first shell information since no higher order shells have to be included in the fitting procedure. To analyze the metal–oxygen contribution to the spectra, the difference file technique was used. In general, the experimental EXAFS spectrum is given as the sum of n individual absorber–backscatterer contributions

$$\chi_{EXP} = \sum_{i=1}^{n} \chi_i$$

and therefore, the contribution due to the jth shell

$$\chi_j = \chi_{EXP} - \sum_{i=1, i\neq j}^{n} \chi_i$$

After subtracting the first metal–metal and metal–oxygen contributions, the remaining signal will be the AXAFS together with the higher order shells. It is now possible to isolate the AXAFS signal by Fourier filtering the data, which removes all higher order contributions. The importance of the use of the low k part of the XAFS spectrum has to be stressed again since it allows a better isolation of the AXAFS contribution from the raw data.

3. Results

3.1. Catalysis

The results for the conversion of neo-pentane at 250°C are given in Table 2. NaY zeolite was progressively NH_4^+ exchanged to reduce the weight percent Na from 10 to 1%. At Na levels of less than about 3 wt.%, the zeolite was thermally unstable and lost crystallinity upon calcination. Thus, stable zeolite supports were obtained with only about half the Na replaced with protons.

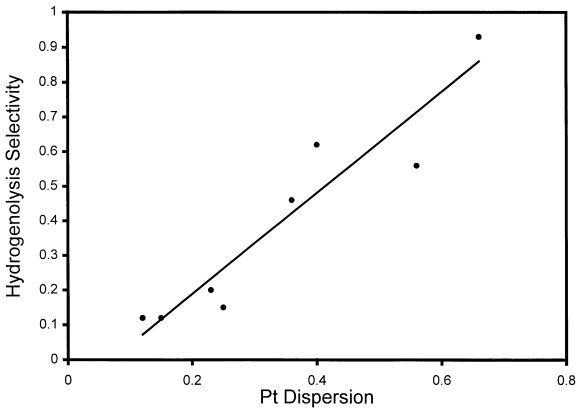

Fig. 4. Hydrogenolysis selectivity vs. the Pt dispersion.

3.1.1. Hydrogenolysis selectivity

Analysis of reaction products by the Delplot method indicated that methane, iso-butane (hydrogenolysis), and iso-pentane (isomerisation) were the primary products. The hydrogenolysis selectivities are reported in Table 2. Fig. 4 shows that the hydrogenolysis selectivity increases linearly with Pt dispersion (decreasing particle size), and appears to be independent of the TOF or composition of the support. Thus, neither the number of protons, La^{3+}, Si/Al ratio nor the non-framework Al strongly affects the hydrogenolysis/isomerisation selectivity.

3.1.2. TOF

Neo-pentane hydrogenolysis is a mono-functional probe reaction, dependent only on the catalytic activity of the metal [37,38] as is confirmed by the primary reaction products: methane, iso-butane (hydrogenolysis), and iso-pentane (isomerisation). Neo-pentane can not undergo a bifunctional mechanism because the neo-pentane molecule can not form an alkene intermediate. Moreover, neo-pentane does not undergo protolytic cracking at the temperatures used for the catalytic reaction (250°C). Therefore, the changes in the TOF can not be ascribed to bifunctional mechanism.

The effects of protons, cation charge, Si/Al ratio and/or extraframework Al results are summarised in Table 4. As observed previously, increasing the number of protons by replacing Na^+ in the support results in an increase in the Pt TOF for neo-pentane conversion [3,9–11,13,20,39,40–42]. The TOF of Pt in H-NaY is 8.5 times higher than that in NaY. H-USY was exchanged with K^+ ions reducing the number of acid sites. As observed for NaY and H-NaY, the TOF of Pt in H-USY is 6.5 times higher than that in K-USY.

NaY was exchanged partially to give 2 wt.% La. Compared to NaY, incorporation of La results in an increase in the TOF of about 25 times (see Table 4). No protons are present in NaLaY. This shows that not only protons but also increasing charge on the cations leads to enhanced activity.

In the absence of protons, the TOF of K-USY is 15.4 times higher than that in Na-Y. Moreover, having about the same number of protons, the TOF of Pt/H-USY is 20 times higher than in Pt/H-NaY (see Table 4). This large increase in the Pt TOF of K-USY compared to NaY demonstrates that an increase in Si/Al ratio and/or the presence of extra-framework Al also leads to an increase in the Pt TOF.

3.2. EXAFS and AXAFS

In Fig. 5a, the raw EXAFS data (k^1 weighted), and in Fig. 5b, the corresponding Fourier transforms (k^2, $\Delta k = 2.5–14\ \text{Å}^{-1}$) of the Pt/NaY sample are shown (measured under hydrogen (solid line) and in vacuum (dotted line). It can clearly be seen from the shift to lower R-values of the imaginary part of the Fourier transform that evacuation causes a shortening of the Pt–Pt bond length. The shoulders at both the low and high R sides of the first Pt–Pt peak in the Fourier transform are due to the non-linear Pt–Pt phase shift and the k dependence of the backscattering amplitude [43]. Fitting of the experimental spectra was done in R-space over the range $R = 1.6–3.1$ Å using a k^2 weighted Fourier transform over the range $k = 2.5–14.0\ \text{Å}^{-1}$. As an example, the Fourier transforms (k^2, $\Delta k = 2.5–14.0\ \text{Å}^{-1}$) of the total fit (dotted line) and raw data (solid line) are shown for the Pt/NaY sample after reduction (Fig. 5c). The differences visible from $0.5\ \text{Å} < R < 1.6\ \text{Å}$ are due to the contributions of AXAFS in the raw data. The coordination parameters as obtained from the EXAFS data analysis are given in Table 5. The other samples have been analysed using the same procedure as described for the Pt/NaY sample after evacuation. The results are also given in Table 5. It can be seen that, after evacuation, the Pt–Pt distance contracts by about 0.1 Å. For the

Table 4
Effect of protons, cation charge, Si/Al ratio and/or extra-framework Al (Al_{EF}) on TOF

Effect	Pt/NaY	Pt/H-NaY	Pt/NaLaY	Pt/K-USY	Pt/H-USY
Protons	1	8.5		1	6.5
Cation charge	1		25.4		
Si/Al and/or Al_{EF}	1	1		20	15.4

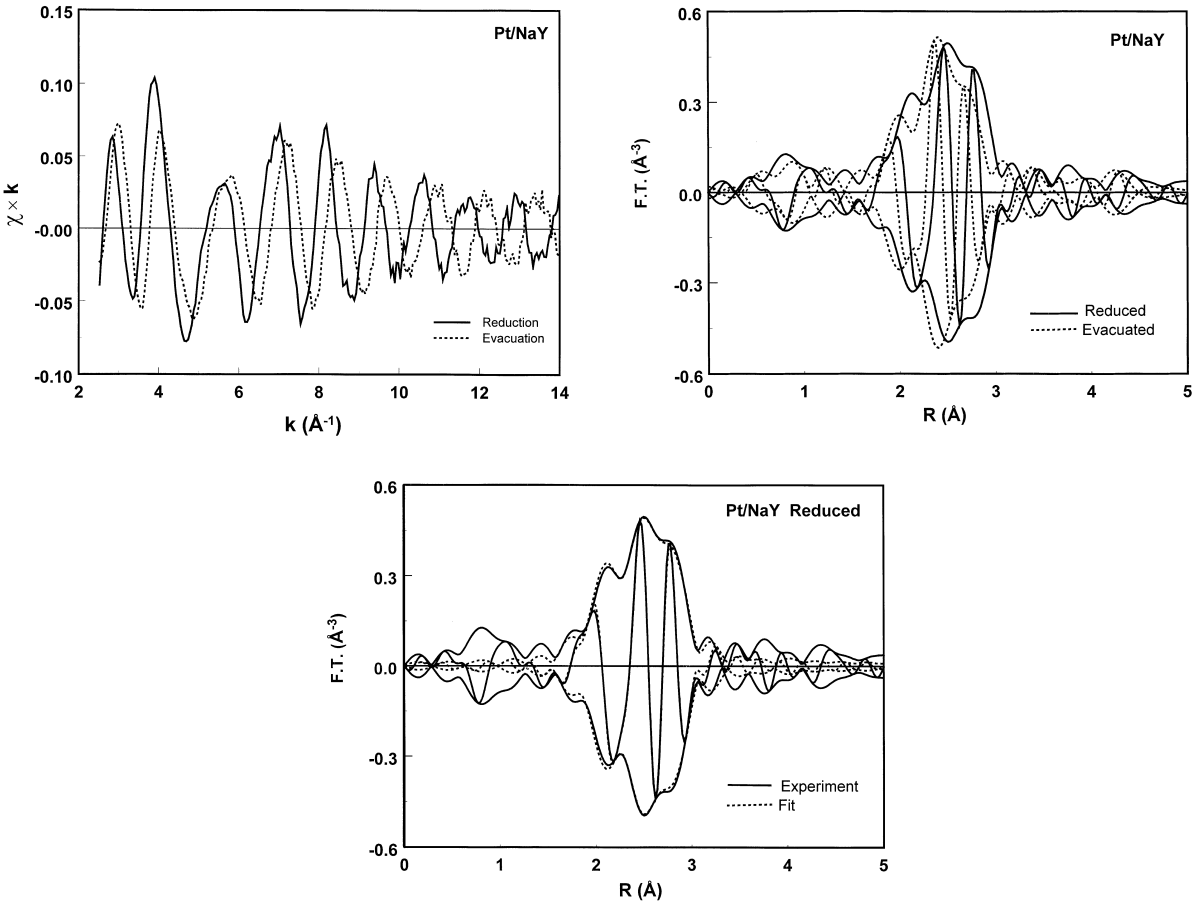

Fig. 5. (a) k^1 weighted EXAFS for PtNaY after reduction in H_2 at 400°C (solid line) and after evacuation at 200°C (dotted line). (b) Fourier transform (k^2 weighted, $2.5\,Å^{-1} < k < 14\,Å^{-1}$) of the data in (a). (c) Fourier transform (k^2 weighted, $2.5\,Å^{-1} < k < 14\,Å^{-1}$) of the raw EXAFS data of Pt/NaY after reduction at 400°C (solid line) and of the model EXAFS (Pt–Pt + Pt–O) obtained by *R*-space fitting ($1.6 < R < 3.1$) (dotted line).

Pt-HUSY sample, a small sintering is observed after evacuation; the Pt–Pt coordination number increases from 5.6 to 6.7. Both after reduction and evacuation, a Pt–O coordination is observed. A long Pt–O coordination distance of 2.65 Å is observed after reduction, which, according to other studies of our group [43–45], is due to the presence of chemisorbed hydrogen in the metal–support interface. After evacuation, the Pt–O distance is shortened to 2.24 Å for Pt/H-USY and to 2.28 Å for Pt/NaY due to the removal of the chemisorbed hydrogen from the metal–support interface [44,45]. HRTEM data collected on the EXAFS

Table 5
Fit results for the Pt/NaY and Pt/H-USY samples. All fittings were done in R-space, k^2 weighting, with 1.6 Å $< R <$ 3.1 Å and 2.5 Å^{-1} $< k <$ 14.0 Å^{-1}. The Debye–Waller factors are relative to the calibrated theoretical references

Coordination	Pt–Pt				Pt–O			
EXAFS parameters	N	R (Å)	$\Delta\sigma^2$ (Å^2)	E_0 (eV)	N	R (Å)	$\Delta\sigma^2$ (Å^2)	E_0 (eV)
Pt/NaY (reduction)	5.4	2.75	0.004	3.3	0.4	2.65	−0.002	−3.0
Pt/NaY (evacuation)	5.5	2.64	0.005	4.4	0.6	2.24	0.008	5.3
Pt/H-USY (reduction)	5.6	2.75	0.002	1.9	1.1	2.65	0.010	1.2
Pt/H-USY (evacuation)	6.7	2.66	0.007	2.9	0.3	2.28	0.008	−3.3

samples have shown that the Pt particles are dispersed inside the zeolite with a particle size distribution of 8–15 Å in diameter, which corresponds with the coordination numbers as obtained with the EXAFS data analysis. HRTEM studies on the samples used for the catalytic experiments show bi-modal distributions with part of the metal particles outside the zeolite crystals, which explains the lower dispersions. Realising that the smaller Pt particles contribute most to the catalytic active surface, special XAFS model catalysts using the same zeolite material as support (see also Table 1) were prepared with all Pt particles dispersed inside the zeolite.

The AXAFS contribution has been isolated by subtracting the calculated Pt–Pt and Pt–O contributions from the raw EXAFS data. The amplitude of the AXAFS function decreases fast with increasing k values and is within the noise level for $k > 8$ Å^{-1}. The k^1 weighted Fourier transform of the difference file is, therefore, taken from 2.5 to 8 Å^{-1} (see Fig. 6). It can be seen that the amplitude of the AXAFS peak in the Fourier transform is larger for Pt/H-USY than for Pt/NaY. Moreover, the peak maximum shifts to lower R values for the Pt/H-USY sample.

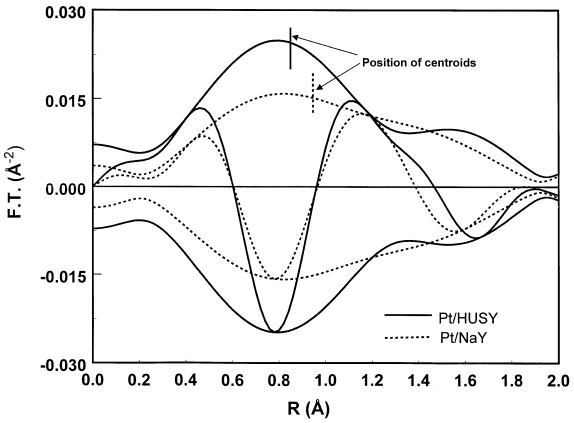

Fig. 6. Comparison of the Fourier transform (k^1 weighted, 2.5 Å^{-1} $< k <$ 8 Å^{-1}) of the AXAFS for Pt/H-USY (solid line) and Pt/NaY (dotted line).

3.3. Shape resonance

In Fig. 7, the normalised L_3 and L_2 edges, respectively, of the Pt/NaY sample after reduction (solid line) and after evacuation (dotted line) are shown. The sample after reduction is further denoted by H–Pt and after evacuation by Pt. The energy scale in Fig. 7 is relative to the edge set at 0.6 times the step height of the Pt sample. The L_2 edge of H–Pt was aligned with the L_2 edge of Pt. The L_3 edges of H–Pt and Pt were shifted so that the EXAFS oscillations in the energy range 50–400 eV are aligned for both L_3 and L_2 edges. This procedure removes the effects of the initial and final states as is further explained in detail in [22]. It can be seen in Fig. 7 that chemisorption of hydrogen changes the shape and intensity of the near edge spectra of both L_2 and L_3 edges.

The AS shape resonance can be isolated by using the subtraction procedure as has been discussed extensively in [22,23]. The results are displayed in Fig. 8 for Pt/H-USY and Pt/NaY, respectively. Both the position and the shape of the AS resonance are very different for both samples. The shape resonance can be fitted using the expression as given in Eq. (1) for a Fano-type line shape. The fits are shown in Fig. 8 with dotted lines. The values for the parameters, which describe the Fano-type line shape, are given in Table 6. It can be seen that the value of E_{res}, which is the difference in energy between the AS state and the Fermi

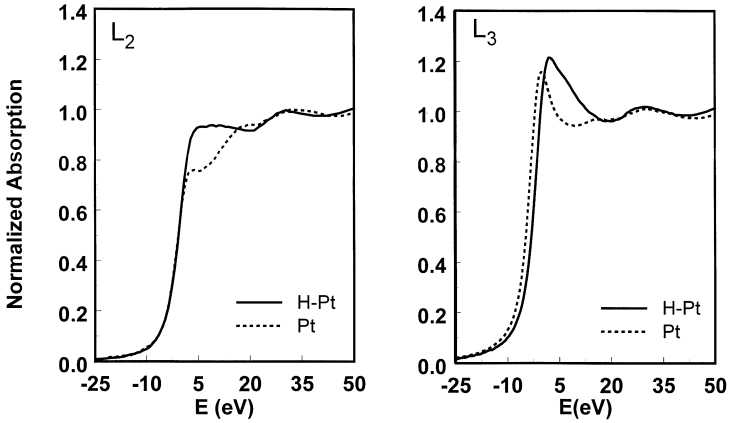

Fig. 7. Comparison of the L_2 and L_3 X-ray absorption edges (aligned as described in the text) for Pt/NaY after reduction in H_2 (H–Pt) and after evacuation (Pt).

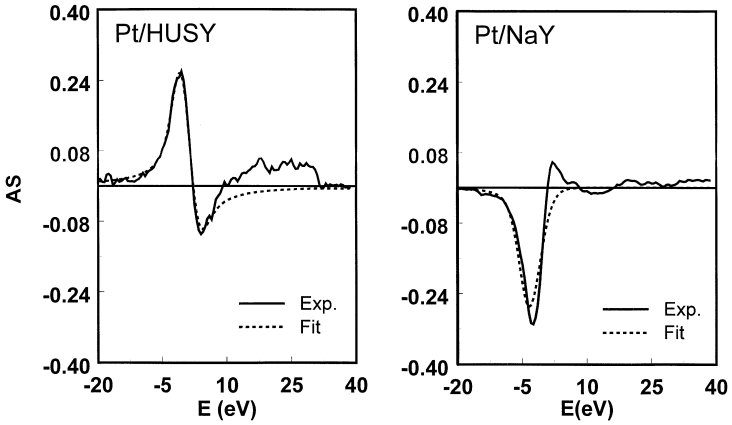

Fig. 8. Comparison of the AS shape resonance extracted from the experimental data as described in the text with the fit of the Fano profile (Eq. (1)) for Pt/HUSY and Pt/NaY.

level, changed by 4.7 eV for these samples. With this large difference in E_{res}, the phase factor Φ changes by approximately $\pi/2$, so that the Fano profile changes by a factor of approximately -1.

4. Discussion

4.1. Catalysis

The increase in TOF of Pt in NaY and K-USY with increasing number of protons (and decreasing number of Na^+/K^+) is in agreement with other studies [3,9–13,20,35–38]. Although the TOF of Pt in H-USY is higher than that in H-Y, the enhancement in the TOF with the number of protons is similar in both zeolites. Like protons, incorporation of polyvalent cations also leads to an enhancement in the Pt TOF. In order to determine the effect of polyvalent cations on the TOF, it is necessary to compare catalysts with an equivalent number of protons since the TOF is dependent on the number of protons. Previously, Ca and La ions were reported to increase the TOF of Pt in Y [46]. It is well known, however, that La ion exchange also leads to the introduction of protons [47,48]. Thus, the previously reported higher activities could be due to the presence of protons, rather than due to polyvalent cations. Fig. 9 compares the TOF of Pt in NaY, K-USY and 2 wt.% LaY. Each zeolite has very few protons, ca. 0.2 mmol g^{-1}. As seen in Fig. 9, the TOF of Pt in

Table 6
Fit parameters obtained from the non-linear least squares fit of Fano profile to the hydrogen induced shape resonance in experimental spectra: the expression $\Phi = \alpha + \beta E_{res}$ with $\alpha = -0.3$ and $\beta = 0.38$ was utilised to reduce the number of parameters [21]. Applied experimental width: Gaussian, 5 eV

Catalyst	A ($\pm$0.03)[a]	E_{res} (eV)[b] ($\pm$0.3)	Width Γ (eV) ($\pm$0.4)	Φ (calculated) ($\pm$0.1)
H-Pt/NaY	0.47	−3.62	5.0	−1.7
H-Pt/H-USY	0.37	1.1	5.0	0.1

[a] Estimated uncertainty in each case.
[b] Relative to the L_2 absorption edge.

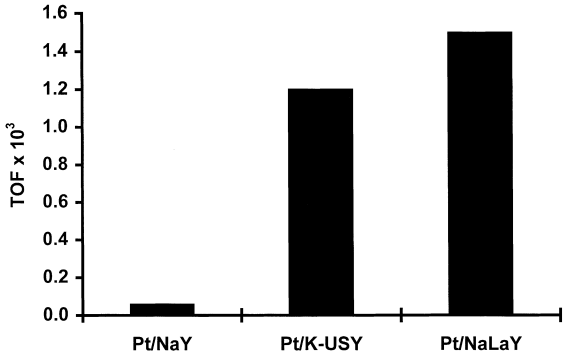

Fig. 9. Comparison of experimentally determined hydrogenolysis TOF's for Pt/NaY, Pt/NaLaY and Pt/K-USY (all samples have the same number of protons).

NaY is significantly lower than the other zeolites. As with LaY, there is a large increase in the TOF of Pt in K-USY compared to that in NaY. Since neither has a significant number of protons, it suggests that an increasing Si/Al ratio and/or non-framework Al in USY has a similar effect on the Pt TOF as La ions.

It has previously been proposed that a fraction of the non-framework Al is cationic and present on ion exchange sites in H-USY [49]. Al NMR of LaY and USY is consistent with this proposal. In LaY, as the cation level increases, the intensity of the 30 ppm peak in the Al NMR increases [50]. Two-dimensional (2D) and multiple quantum (MQ) NMR indicate that the 30 ppm peak is due to a quadrapolar distortion of the tetrahedral resonance of a (lattice) Al exchanged by a La^{3+} ion [51]. Similarly, in USY, the 30 ppm Al NMR resonance may be due to a fraction of the non-framework Al present as cations with sufficient charge to distort the tetrahedral NMR resonance. In addition to NMR, comparison of the number of framework Al determined by XRD with the number of acid sites by TPD of NH_3 indicates that approximately 30% of the lattice Al in H-USY is non-acidic, i.e. exchanged by non-framework Al cations [52]. More work is required to confirm whether some of the non-framework Al in USY is present as a polyvalent cations. However, it is clear that, in the absence of support acidity, an increasing Si/Al ratio and/or the presence of non-framework Al results in an increase in the Pt TOF similar in magnitude to that of La^{3+} ions.

4.2. Structure of Pt particles

The metal particles in both Pt/NaY and Pt/H-USY catalysts are small with first shell Pt–Pt co-ordination numbers around 5.5; i.e. the average metal particle consists of approximately 15 atoms. In the presence of chemisorbed hydrogen, the Pt–Pt distance of 2.75 Å is characteristic of metallic Pt. Under vacuum, the Pt–Pt distance contracts due to rehybridisation of the metal spd orbitals [53,54]. Oxygen ions in these small Pt particles are detected within the first co-ordination sphere, but neither sodium, silicon, nor aluminium ions were found within 3 Å of the platinum particles for either catalyst. Since the Pt particles in both catalysts have the same structural properties, we conclude that the change in the catalytic properties of the metal particles is due to a change in the electronic properties on the oxygen ions of the support.

4.3. AXAFS and Pt–H anti-bonding shape resonance

For Pt in H-USY zeolite, the intensity of the AXAFS peak is larger and the centroid is shifted to lower R in comparison with Pt/NaY (see Fig. 6). Comparison of the fitting parameters in Table 6 indicates that E_{res} in Pt/NaY is 4.7 eV lower than in Pt/H-USY, where E_{res} is the difference in energy between the Fermi level and the Pt–H anti-bonding orbital. Comparing Pt/NaY to Pt/H-USY, it is seen that two of the three parameters discussed in Table 4 (proton density, Si/Al

ratio and/or extra-framework Al) have changed. The results published by Mojet et al. [23,24] for Pt/LTL catalysts showed that the AXAFS intensity and the E_{res} increased with increasing proton density. These results are consistent with the results presented here. However, based upon the TOF results presented in Table 4, it is very likely that the increase in Si/Al ratio and/or the presence of extra-framework Al in H-USY may also be responsible for increasing the AXAFS intensity and E_{res}. Strong support for this comes from the increase in the Al AXAFS intensity detected on the framework Al in H-USY [55] in comparison with H-NaY, which was attributed to the increase in Si/Al ratio and/or extra-framework Al. As will be shown below, the increase in the AXAFS and E_{res} reflect the same effect; namely the increase in charge of the oxygen ions of the support.

4.4. Madelung potential of zeolite support

Several studies have shown that exchange of NaY by La^{3+} or H^{+} ions results in an increase in the O, Si and Al XPS binding energies [56,57]. Recently, a theoretical study presented evidence that the origin of these shifts to higher binding energy lies in the changes in Madelung potential [57], rather than in a charge transfer between the ions of the zeolite lattice. Calculations of the Madelung potential predict that there is an increase in the O, Si, and Al binding energies in zeolites with increasing Si/Al ratio similar to the experimentally determined values. Generally, the support composition determines the Madelung potential. The Madelung potential determines the surface potential of the oxide ions. The consequence of the model put forward by Mojet et al. [23], and our new results here, is that the influence of Na^{+}, H^{+}, La^{3+}, extra framework Al ions and changing Si/Al ratio leads to a change in the electron distribution or charge on the support oxygen ions.

4.5. Evidence for the nature of the metal–support interaction

As shown above, the AXAFS and the Pt–H anti-bonding shape resonance depend on the support properties. Further, the support properties determine through the Madelung potential the charge on the support oxygen ions. It will be shown here, discussed in terms somewhat different from that published previously [21–23], how the charge of the support oxygen atoms influences the electronic structure of the Pt particles as well as how the Pt–H bonding is affected.

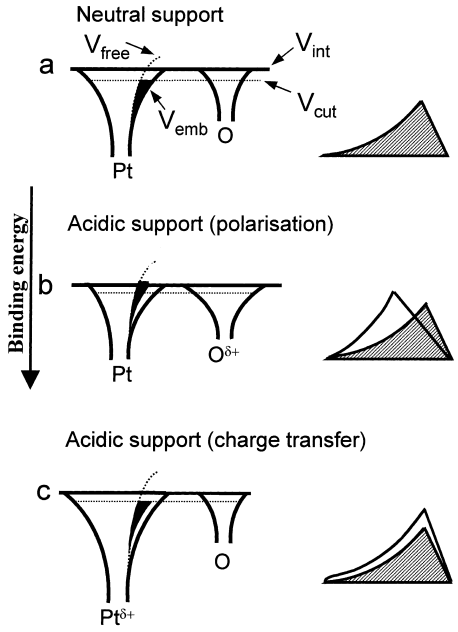

Fig. 10. Schematic potential curves appropriate for a neutral and an acidic support assuming polarisation of the cluster by the support (Fig. 10b) or actual charge transfer from the cluster to the support (Fig. 10c). Note that the O or Pt atom with the δ^{+} charge is shown with a longer range Coulomb potential. The hatched area on the right-hand side illustrates the expected FT of the AXAFS for the neutral support in all cases. The dark shaded area is proportional to V_{free} minus V_{emb} for the neutral support and is taken as a reference. In Fig. 10b, all Pt energy levels are at a higher binding energy. As shown, a shift to lower R of the centroid is expected assuming polarisation of the cluster by the support; no shift assuming charge transfer.

Fig. 10a and b compare the difference in the Pt–O interatomic potential as the charge on the oxygen ion increases. Increasing the charge on oxygen will change the shape of the potential of platinum since the interaction with oxygen will move platinum electrons nearer to oxygen. This is illustrated in Fig. 10b by the larger Coulomb tail on the O atom with increased charge, and hence, more 'roll over' of the interatomic potential and the lowering of V_{cut}. This causes a larger difference between V_{emb} and the free atom potential, i.e. increase in the amplitude of the Fourier transform of

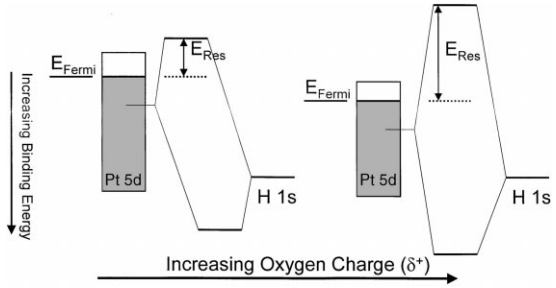

Fig. 11. Molecular orbital (MO) scheme of Pt–H interaction showing changes as a function of support oxygen charge. As the O charge increases, the Pt ionisation potential increases (as indicated by the AXAFS) and the Pt 5d band narrows. This causes the Pt–H bond to become less ionic (or more covalent) with a corresponding increase in E_{res}.

the AXAFS oscillations and a shift of the maximum intensity to lower *R* values. At the same time, the platinum valence d orbitals are moved to higher binding energy; i.e. the ionisation potential of Pt is increased. Moreover, the Pt d-orbitals are radially contracted and the width of the d-band is reduced, resulting in less 'metallic' character. This is also reflected in the XPS 3d core level shift of Pd particles dispersed in LTL [13] and in the increase in the linear/bridge ratio of the CO FTIR spectra of Pd/LTL, Pt/LTL and Pt/SiO_2 [20].

Fig. 11 illustrates how these changes in the Pt electron distribution (both energy and spatial) influence the Pt–H bonding. The energy of the H 1s orbital is lower than the energy of the Pt valence orbitals [27] and does not change with catalyst composition. The more similar the energy of the Pt and H orbitals with increasing charge on the oxygen ions, the more covalent and stronger the Pt–H bond becomes, and the greater the difference in energy between the Pt–H anti-bonding orbital and the Fermi level, i.e. larger E_{res} (see Fig. 11). The implication from the shape resonance analysis is that the energy of the Pt valence d-orbitals affects the chemisorption energy of the adsorbate.

4.6. Comparison with previously proposed models for the metal–support interaction

The model for the metal–support interaction as discussed above indicates that an actual charge transfer from the metal to the support with increasing charge on the oxygen ions does not occur. This is illustrated in Fig. 10c, where, assuming that such a charge transfer does occur, the oxygen potential is the same as in Fig. 10a. The charge on Pt now creates the long range Coulomb tail on the Pt atom. This results in no change in the position of the maximum in the AXAFS, in contrast to that found experimentally. Thus, the AXAFS results are in agreement with other arguments given by Ponec et al. [17] according to which charge transfer is very unlikely.

Previously, it has been proposed that cations induce a polarisation of the metal cluster, implying movement of charge within the cluster, which results in an electronic dipole across the cluster [18,19]. This is illustrated in Fig. 12a, where O polarisation produces a net increase in the final electron binding energy of the cluster. For the monolayer configuration of Pt atoms as given in Fig. 12b, no such dipole across the cluster is induced. The AXAFS cannot distinguish between these two extreme cases since it gives the average over all Pt atoms. Therefore, the AXAFS cannot exclude polarisation of the cluster by the O support atoms, and for larger metallic clusters, such polarisation is expected. Thus, the AXAFS results for large metal particles (50 atoms) on flat amorphous supports [58] (similar to the case in Fig. 12a), smaller particles dispersed in Y zeolite reported here, and very small particles (four to six atoms) dispersed in zeolite LTL [23,24] (the case in Fig. 12b), all show similar trends with increasing charge density (δ^+) on the support oxygen ions. Therefore, the essence of the metal–support interaction is not the inducement of a dipole across the metal particle, but the increase in average d-orbital binding energy of the metal particle with increasing charge (δ^+) on the support oxygen ions.

5. Conclusions

Previously, the combined interpretation of the catalytic activity, EXAFS structural analysis, XPS, FTIR of chemisorbed CO, XANES shape resonance and AXAFS in Pt/LTL led to the proposal of a new model describing the metal–support interaction in supported noble metal catalysts [23,24]. It was suggested that the metal ionisation potential decreases with increasing alkalinity of the support. The primary interaction is a Coulomb attraction between the metal particles

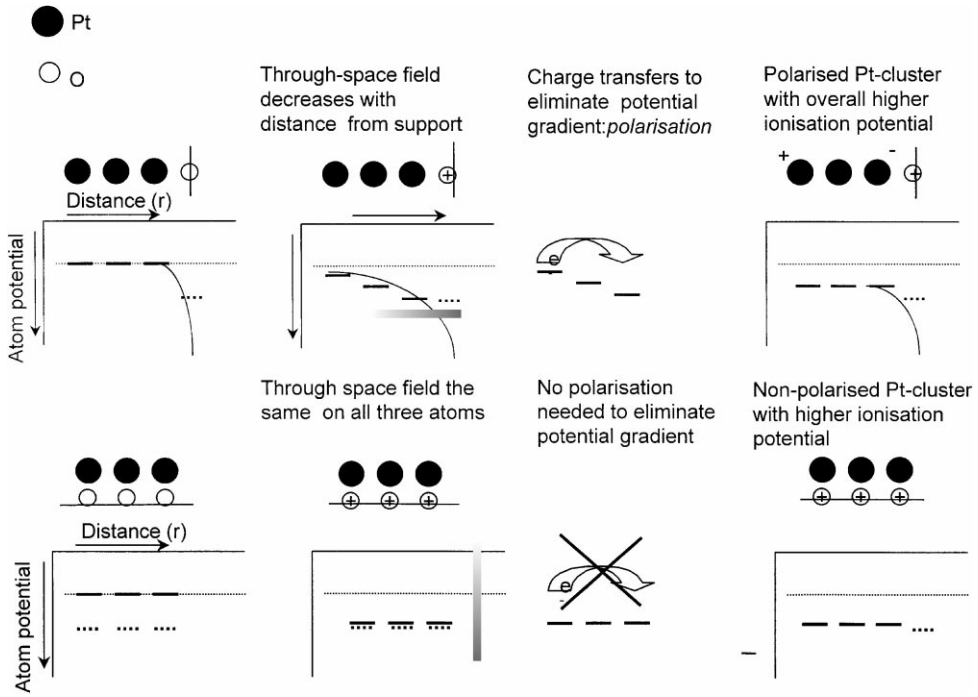

Fig. 12. Schematic showing the polarisation of the Pt atoms by the support O atoms, and the response of the cluster to this polarisation. The top portion illustrates movement of charge from the outer Pt atoms towards the O atom assuming the cluster is metallic, similar to that suggested by van Santen [17,18]. The bottom portion shows the case when little interatomic movement of charge occurs because the thickness of the cluster is small compared to the potential change. AXAFS cannot differentiate between these two cases because it reflects the average increase in ionisation potential for the cluster, which will be significantly larger in the latter case.

and support oxygen ions. The support interaction leads to a change in the interatomic potential of metal valence orbitals, resulting in a higher metal binding energy in acidic supported catalysts, for example. This shift in energy of the valence orbitals directly affects the chemisorption energy of adsorbates, resulting in changes in the catalytic and spectroscopic properties. This interatomic potential model explicitly excludes the need for electron transfer.

In the previous study [23], the electronic structure of the Pt particles was altered by changing the acidity/alkalinity of the LTL zeolite. The results from the current study demonstrate that the oxygen binding energy, and hence, the catalytic and spectroscopic properties of the metal particles, can also be changed by altering other properties of the support, such as the Si/Al ratio, polyvalent cations, and non-framework promoter atoms. In the absence of Brønsted acid sites, exchange with polyvalent cations in zeolites leads to an increase in the metal TOF. More generally, in amorphous supports and with catalytic promoters, the oxygen binding energy is determined by the charge on the metal ion and the number of oxygen neighbors. By control of the compositions of oxide support, it is expected that the catalytic properties can be tailored to give new catalysts with improved properties.

Acknowledgements

We like to acknowledge the EU large scale facilities programme, which makes the XAFS experiments at the SRS, Daresbury possible.

References

[1] P. Well, Oil and Gas Journal Data Book, Tulsa, 1994.
[2] B.C. Gates, Supported metal clusters: synthesis, structure and catalysis, Chem. Rev. 95 (1995) 511.

[3] R.A. Dalla Betta, M. Boudart, in: J.W. Hightower (Ed.), Proc. 5th Int. Cong. Catal., 20-20 August 1972, Miami Beach, Florida, vol. 2, North Holland, Amsterdam, 1973, p. 1329.
[4] F. Figuera, J.R. Gomex, M. Primet, Adv. Chem. Ser. 121 (1973) 480.
[5] S.D. Lin, M.A. Vannice, J. Catal. 143 (1993) 539.
[6] M. Vaarkamp, J.T. Miller, F.S. Modica, G.S. Lane, D.C. Koningsberger, in: Proc. 10th Int. Cong. on Catal., Budapest, 1992, p. 809.
[7] J.T. Miller, F.S. Modica, B.L. Meyers, D.C. Koningsberger, Prep. ACS Div. Petr. Chem. 38 (1993) 825.
[8] Z. Karpinski, S.N. Gandhi, W.M.H. Sachtler, J. Catal. 141 (1993) 337.
[9] S.T. Homeyer, Z. Harpinski, W.M.H. Sachtler, J. Catal. 123 (1990) 60.
[10] G. Larsen, G.L. Haller, Catal. Lett. 3 (1989) 103.
[11] A. de Mallmann, D. Barthoumeuf, J. Chem. Phys. 87 (1990) 535.
[12] A. de Mallmann, D. Barthoumeuf, Stud. Surf. Sci. Catal. 46 (1989) 429.
[13] B.L. Mojet, M.J. Kappers, J.C. Meyers, J.W. Niemantsverdriet, J.T. Miller, F.S. Modica, D.C. Koningsberger, Stud. Surf. Sci. Catal. 84 (1994) 909.
[14] A.Y. Stakheev, W.M.H. Sachtler, J. Chem. Soc., Faraday Trans. 87 (1991) 3703.
[15] M. Sugimoto, H. Katsuno, T. Hayasaka, N. Ishikawa, K. Hirasawa, Appl. J Catal. A., Gen. 102 (1993) 167.
[16] Z. Zhang, T.T. Wong, W.M.H. Sachtler, J. Catal. 128 (1991) 13.
[17] V. Ponec, G.C. Bond, Catalysis by metals and alloys, Stud. Surf. Sci. Catal. 95 (1995) 234.
[18] A.P. Jansen, R.A. van Santen, J. Phys. Chem. 94 (1990) 6764.
[19] E. Sanchez-Marcos, A.P.J. Jansen, R.A. van Santen, Chem. Phys. Lett. 16 (1990) 399.
[20] B.L. Mojet, M.J. Kappers, J.T. Miller, D.C. Koningsberger, in: Proc. 15th Int. Cong. Catal., Baltimore, MD, 1996.
[21] D.E. Ramaker, B.L. Mojet, D.C. Koningsberger, W.E. O'Grady, J. Phys.: Condens. Matter 10 (1998) 8753.
[22] D.E. Ramaker, B.L. Mojet, M.T. Garriga Oostenbrink, J.T. Miller, D.C. Koningsberger, Phys. Chem. Chem. Phys. 1 (1999) 2293.
[23] B.L. Mojet, D.E. Ramaker, J.T. Miller, D.C. Koningsberger, Catal. Lett. 62 (1999) 15.
[24] B.L. Mojet, J.T. Miller, D.E. Ramaker, D.C. Koningsberger, J. Catal. 186 (1999) 373.
[25] N.A. Bhore, M.T. Klein, K.B. Bischoff, Ind. Eng. Chem. Res. 29 (1990) 313.
[26] L.F. Mattheiss, R.E. Dietz, Phys. Rev. B 22 (1980) 1663.
[27] B. Hammer, J.K. Nørskov, Nature 376 (1995) 238.
[28] B.W. Holland, J.B. Pendry, R.F. Pettifer, J. Bordas, J. Phys. C: Solid State Phys. 11 (1978) 633.
[29] J.J. Rehr, C.H. Booth, F. Bridges, S.I. Zabinsky, Phys. Rev. B 49 (1994) 12347.
[30] M. Vaarkamp, B.L. Mojet, F.S. Modica, J.T. Miller, D.C. Koningsberger, J. Phys. Chem. 99 (1995) 16067.
[31] J.W. Cook, D.E. Sayers, J. Appl. Phys. 52 (1981) 5024.
[32] G.E. van Dorssen, D.E. Ramaker, D.C. Koningsberger, Phys. Rev. B, submitted for publication.
[33] S.I. Zabinsky, J.J. Rehr, A. Ankudinov, R.C. Albers, M.J. Eller, Phys. Rev. B 52 (1995) 2995.
[34] R.W.G. Wyckoff, Crystal Structures, 2nd ed., vol. 1, Wiley, New York, 1963.
[35] M. Trömel, E. Lupprich, Z. Anorg. Chem. 160 (1975) 414.
[36] M. Vaarkamp, J.C. Linders, D.C. Koningsberger, Physica B 208/209 (1995) 159.
[37] S.M. Davis, G.A. Somorjai, in: D.A. King, D.P. Woodruff (Eds.), The Chemical Physics of Solid Surfaces and Heterogeneous Catalysts, vol. 4, Elsevier, Amsterdam, 1982, p. 271.
[38] J.R. Anderson, N.R. Avery, J. Catal. 16 (1967) 315.
[39] W.M.H. Schachtler, A.Y. Stakheev, Catal. Today 12 (1992) 283.
[40] D.L. Shawn, M.A. Vannice, J. Catal. 143 (1993) 539.
[41] D.L. Shawn, M.A. Vannice, J. Catal. 143 (1993) 554.
[42] J.T. Miller, D.C. Koningsberger, J. Catal. 162 (1996) 209.
[43] M. Vaarkamp, F.S. Modica, J.T. Miller, D.C. Koningsberger, J. Catal. 144 (1993) 611.
[44] M. Vaarkamp, F.S. Modica, J.T. Miller, D.C. Koningsberger, J. Catal. 163 (1996) 294.
[45] D.C. Koningsberger, F.B.M. van Zon, M. Vaarkamp, A. Muñoz-Paez, in: Y. Iwasawa (Ed.), X-ray Absorption Fine Structure for Catalysts and Surfaces, Series on Synchrotron Radiation Techniques and Applications, vol. 2, World Scientific, Singapore, 1996, p. 257.
[46] K. Foger, J.R. Anderson, J. Catal. 54 (1978) 318.
[47] J.W. Ward, J. Catal. 10 (1968) 34.
[48] A.P. Bolton, J. Catal. 22 (1971) 9.
[49] F. Lonyi, J.H. Lunsford, J. Catal. 136 (1992) 566.
[50] H. Klein, H. Fuess, M. Hunger, J. Chem. Soc., Faraday Trans. 91 (1995) 1813.
[51] J.A. van Bokhoven, A.L. Roest, A.P.M. Kentgens, D.C. Koningsberger, in: M.M.J. Treacy, B.K. Marcus, M.E. Bisher, J.B. Higgins (Eds.), Proc. 12th Int. Zeolite Conference, vol. 4, Baltimore, 1999, p. 2515.
[52] M.A. Kuehne, H.H. Kung, J.T. Miller, J. Catal. 171 (1997) 293.
[53] B. Delly, D.E. Ellis, A.J. Freeman, E.J. Baerends, D. Post, Phys. Rev. B 27 (1983) 2132.
[54] A. Balerna, S. Mobilio, Phys. Rev. B 34 (1986) 2293.
[55] D.C. Koningsberger, J.A. van Bokhoven, J. de Graaf, D.E. Ramaker, submitted for publication.
[56] Y. Okamoto, M. Ogawa, A. Maezawa, T. Imanaka, J. Catal. 112 (1988) 427.
[57] W. Grunert, M. Muhler, K.-P. Schroder, J. Sauer, R. Schlögl, J. Phys. Chem. 98 (1994) 10920.
[58] M.K. Oudenhuijzen, J.T. Miller, D.E. Ramaker, D.C. Koningsberger, submitted for publication.